Macromolecules **2002,** *35,* 2417−2422

Crystallization-Induced Deformation of Spherical Microdomains in Block Copolymer Blends Consisting of a Soft Amorphous Phase

Hsin-Lung Chen,*,[†] Hsiu-Chun Li,[†] Yen-Yu Huang,[†] and Fang-Chyou Chiu[‡]

Department of Chemical Engineering, National Tsing Hua University, Hsin-Chu, Taiwan 30013, R.O.C., and Department of Chemical and Materials Engineering, Chang Gung University, Kweisan, Taiwan 333, R.O.C.

Received October 8, 2001
Revised Manuscript Received December 11, 2001

Introduction

Crystalline−amorphous (C−A) block copolymers have received increasing attention in recent years due to the complicated structural patterns and phase transformation process driven by the combined effect of crystallization and interblock incompatibility (microphase separation). We consider the case where C block is the minor constituent with crystallization window situating below the order−disorder transition temperature (T_{ODT}) prescribed by the interblock incompatibility; crystallization in this case occurs within the nanoscaled microdomains (consisting of C blocks) templated by the prior microphase separation in the melt state.

Despite being a minor component, crystallization of C blocks in the microdomains may sometimes perturb the preexisting melt structure depending on the driving forces of crystallization and microphase separation as well as the T_g of the amorphous blocks ($T_g{}^a$).[1−14] When $T_g{}^a$ lies above the crystallization temperature (T_c), the melt structure in terms of the long-range order and the geometric characteristics (e.g., shape, size) of the microdomains is expected to be preserved after crystallization.

Perturbation of melt structure becomes accessible when the system contains a soft amorphous phase at T_c (i.e., when $T_c \gg T_g{}^a$). The extent of perturbation now depends on the ability of the crystallization driving force to dominate over the driving force of microphase separation that stabilizes the molten mesophase.[10,12] The melt structure may still retain in strongly segregated systems where the driving force of microphase separation outweighs that of crystallization.[12] In the cases of weakly segregated systems where the crystallization driving force may easily overwhelm the driving force of microphase separation, both the long-range order and geometric characteristics of the microdomains associated with the preexisting morphology may be destroyed and transformed into those associated with the crystalline morphology where one-dimensionally stacked lamellae consisting of alternating crystalline and amorphous layers has been predominantly identified.[2,5,6,12] If the molten microdomains are cylinders or spheres, transformation into such a lamellar structure must involve long-range coalescence or welding of the individual domains during crystallization. The mechanism of such a microdomain welding is not well understood so far. Nojima et al. studied the transformation of spherical microdomains into lamellar structure induced by the crystallization of polycaprolactone (PCL) blocks in PCL-*block*-polybutadiene (PCL-*b*-PB).[5] The microdomain welding was proposed to be triggered by the crystal growth where a crystal embryo appeared independently in one of the spherical domains, and it grew by absorbing the molten PCL blocks in other microdomains onto the growing surface.

It should be noted that the above discussion considers only the extreme conditions where the crystallization driving force is either able or unable to overwhelm the driving force of microphase separation. There may exist what we call the "intermediate regime" where the morphology after crystallization arises from the balance between the driving forces of these two self-organizing processes. The molten mesophase in this case is neither fully preserved nor completely transformed into 1-D stacked lamellae, but instead the "intermediate structures" are generated through the crystallization process. In this study, we probe the crystalline microdomain structure in the diblock copolymer blends of a poly(ethylene oxide)-*block*-polybutadiene (PEO-*b*-PB) and a PB homopolymer. A PEO-*b*-PB was blended with a low molecular weight PB homopolymer to yield the wet-brush type of blends containing PEO spheres in the melt.[14−17] Crystallizations of the PEO blocks within the spherical microdomains were induced at the temperatures above the T_g of PB such that the domains were dispersed in a soft matrix during crystallization. The microdomain structures were then probed by small-angle X-ray scattering (SAXS) from which the perturbation in domain structure was resolved through the analysis of the form factor scattering. It will be shown that the spherical microdomains slightly deformed into ellipsoid-like objects upon crystallization.

Experimental Section

PEO-*b*-PB with the polydispersity index (M_w/M_n) = 1.04 was synthesized by sequential anionic polymerization of butadiene and ethylene oxide (Polymer Source, Inc.). M_n of the PEO and PB blocks was 6000 and 20 400, respectively. The 1,4-addition PB homopolymer with $M_n = 1000$ and $M_w/M_n = 1.04$ was also synthesized by anionic polymerization (Polymer Source, Inc.). Microphase-separated PEO-*b*-PB/PB blends were prepared by solution mixing using toluene as the cosolvent, followed by removing the solvent in vacuo at 80 °C. Two blend compositions with the overall PEO volume fractions (f_{PEO}) of 0.13 and 0.17 (denoted by 1K13 and 1K17, respectively) were prepared.

Crystallizations were conducted by two processes: (1) slow crystallization where the blends were cooled from 85 °C (T_m of PEO < 85 °C < T_{ODT}; T_{ODT} > 200 °C) to −50 °C at −5 °C/min and (2) rapid crystallization where the samples were directly quenched from 85 °C to −50 °C followed by crystallization at this temperature for 1 h. The crystallinities of the samples subjected to these two crystallization processes are tabulated in Table 1.

SAXS was utilized to probe the morphology of amorphous and crystalline PEO-*b*-PB/PB blends. The amorphous samples were prepared by first annealing at 85 °C for 5 min followed by cooling to room temperature; PEO blocks remained amorphous upon the cooling in that the degree of undercooling at room temperature ($\Delta T \approx 35$ K) was insufficient to initiate any detectable trace of crystallization (crystallization in the spherical microdomains had to proceed through a homogeneous nucleation which required exceedingly large undercooling (ΔT > 90 K)).[14,15] All SAXS measurements were performed at room temperature. The X-ray source, an 18 kW rotating anode X-ray

---

[†] National Tsing Hua University.
[‡] Chang Gung University.
* To whom correspondence should be addressed.

10.1021/ma011748k CCC: $22.00

Table 1. Crystallinities (X_c) and Melting Points (T_m) of Crystalline PEO-*b*-PB/PB Blends Subjected to the Two Crystallization Processes

sample	crystallization process[a]	X_c[b]	T_m (°C)
1K17	SC	0.74	54.8
	IX	0.76	55.1
1K13	SC	0.73	53.0
	IX	0.74	51.5

[a] SC and IX signify that the crystallizations were conducted by cooling the blends from 85 to −50 °C at −5 °C/min and by isothermal annealing at −50 °C, respectively. [b] X_c was calculated from the enthalpy of melting (Δh_f) measured by DSC, i.e., $X_c = \Delta h_f/(\Delta h_f^0 w_{PEO})$, with Δh_f^0 (=200 J/g) and w_{PEO} being the bulk enthalpy of melting and weight fraction of PEO, respectively.

generator (Rigaku) equipped with a rotating anode Cu target, was operated at 200 mA and 40 kV. The incident X-ray beam was monochromated by a pyrolytic graphite crystal, and a set of three pinhole inherent collimators were used so that the smearing effects inherent in slit-collimated small-angle X-ray cameras can be avoided. The scattered intensity was detected by a two-dimensional position-sensitive detector (ORDELA Model 2201X, Oak Ridge Detector Laboratory Inc.) with 256 × 256 channels (active area 20 × 20 cm^2 with ∼1 mm resolution). All data were corrected by the background (dark current and empty beam scattering) and the sensitivity of each pixel of the area detector. The intensity profile was output as the plot of the scattering intensity (I) vs the scattering vector, $q = 4\pi/\lambda \sin(\theta/2)$ (θ = scattering angle). All the intensity profiles reported here have also been corrected for thermal diffuse scattering (TDS). The intensity level of TDS was assumed to be a constant, and its magnitude was determined from the slope of the Iq^4 vs q^4 plot.[18]

The real-space morphology of the blends was observed by a JEOL JEM-2000FXZ transmission electron microscope operated at 120 kV. The film specimens were microtomed at −90 °C using a Reichert Ultracut E low-temperature sectioning system. The ultrathin sections were stained with the vapor of 1% $OsO_{4(aq)}$ for 2 h. It should be noted that the originally amorphous samples may undergo crystallization during the ultrathin section preparation at −90 °C; therefore, for the morphological observations of the amorphous samples, the ultrathin sections were annealed at 65 °C for 3 min to melt the PEO crystals prior to OsO_4 staining.

Results and Discussion

Figure 1 shows the SAXS profiles of amorphous and crystalline 1K17 and 1K13 blends. The scattering maxima denoted by "$i = n$" (n = 1, 2, 3, ...) are the form factor peaks associated with the scattering from isolated microdomains.[14] The form factor scattering depends on the geometric characteristics of the microdomains, including the shape, the average dimension, and the dimension distribution. The present crystalline system still exhibits clear form factor maxima, showing that the crystalline domains retain quite well-defined geometry; this is in contrast to polyethylene-*block*-(styrene-*ran*-ethylene-*ran*-butene) (E/SEB)[19] and the previously studied blends with shorter PB blocks, wherein the form factor peaks were smeared out upon crystallization.[14] For 1K17 blend, the primary lattice peak broadens but stays at 0.25 nm^{-1} while the form factor peaks have shifted slightly to higher q upon crystallization. Similar perturbation in SAXS profiles is identified for the 1K13 blend, except that the primary lattice peaks of the crystalline samples are located at slightly higher q than that of the amorphous counterpart. The two crystallization processes appear to generate similar crystalline domain structure, as the scattering profiles are relatively independent of the crystallization history. This also contrasts with the sphere-forming blends with shorter PB blocks, wherein the perturbation in SAXS profiles strongly depends on the rates of crystallization conducted at various temperatures.[20]

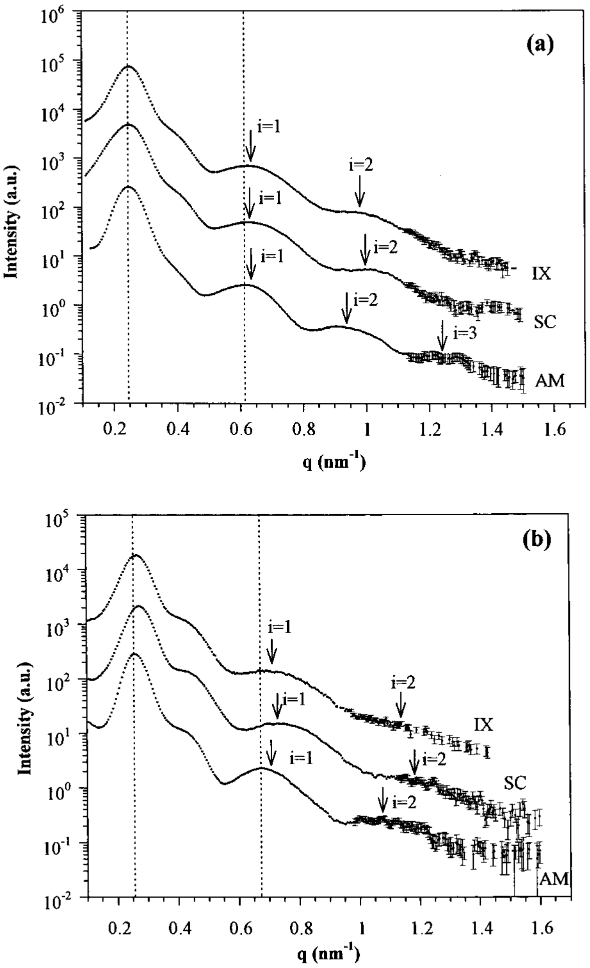

Figure 1. SAXS profiles of amorphous and crystalline PEO-*b*-PB/PB blends: (a) 1K17 composition (f_{PEO} = 0.17) and (b) 1K13 composition (f_{PEO} = 0.13). The scattering curves of the amorphous samples are marked by "AM". Those marked by "SC" and "IX" signify the scattering profiles of the samples crystallized by cooling from the melt to −50 °C at −5 °C/min and by isothermal crystallization at −50 °C, respectively. The form factor peaks are denoted by "$i = n$" with n = 1, 2, 3, ...

Intuitively, the shift of the form factor peaks toward higher q seems normal because crystallization is a densification process which should lead to contraction of the microdomain volume. However, quantitative fitting of the form factor profiles by the model scattering formula reveals subtle perturbations in domain structure besides volume contraction. We first consider fitting of the observed profiles by the independent scattering from spheres. The form factor for an isolated sphere with a diffuse phase boundary is given by[21]

$$f_s^2(q) = [V_{sph}\Delta\rho\Phi(U)]^2 \exp(-\sigma^2 q^2) \qquad (1)$$

where V_{sph} is the volume of the sphere, $\Delta\rho$ is the electron density contrast between the sphere and the matrix, σ is a parameter relating to the thickness of the diffuse phase boundary, and Φ(U) is the scattering function given by

$$\Phi(U) = \frac{3(\sin U - U \cos U)}{U^3} \qquad (2)$$

Table 2. Results of the Fit by Spherical Form Factor for Amorphous and Crystalline PEO-*b*-PB/PB Blends

sample	physical state of PEO blocks[a]	$\langle R\rangle$ (nm)	σ_R (nm)	σ^2 (nm^2)	t_i[b] (nm)	ρ_x (g/cm^3)
1K17	amorphous	9.20	0.75	0.50	1.25	
	crystalline (SC)	8.60	0.90	0.60	1.37	1.37
	crystalline (IX)	8.70	0.90	0.70	1.49	1.32
1K13	amorphous	8.10	0.85	0.35	1.05	
	crystalline (SC)	7.25	0.85	0.70	1.48	1.56
	crystalline (IX)	7.45	1.00	0.70	1.48	1.44

[a] SC and IX signify that the crystallizations were conducted by cooling the blends from 85 to −50 °C at −5 °C/min and by isothermal annealing at −50 °C, respectively. [b] t_i is the thickness of the diffuse phase boundary calculated by $t_i = (2\pi)^{1/2}\sigma$.

where $U = qR$ with R being the radius of the sphere. The distribution of R can be taken into account in calculating the scattering patterns so that the experimentally observed profiles can be simulated more accurately. In this case, the average form factor is given by[22]

$$\langle f_s^{\,2}(q)\rangle = \frac{\int_0^\infty f_s^{\,2}(q)\, P(R)\, \mathrm{d}R}{\int_0^\infty P(R)\, \mathrm{d}R} \tag{3}$$

where $P(R)$ is the distribution function for the sphere radius. The Gaussian distribution function is adopted here for $P(R)$, viz.

$$P(R) \sim \exp\left[\frac{-(R - \langle R\rangle)^2}{2\sigma_R^{\,2}}\right] \tag{4}$$

The values of average radius ($\langle R\rangle$), width of distribution (σ_R), and σ^2 obtained from the fit by eq 3 are listed in Table 2, and the corresponding calculated form factor profiles are plotted in Figure 2. The calculated profiles closely match the observed ones for all samples although slight deviations may be found for crystalline 1K17 at $q > 1.15$ nm^{-1}. From the average radii obtained, the densities of the crystalline spheres were calculated to see whether spherical form factor prescribes reasonable densities to the crystalline microdomains. The density of the crystalline sphere, ρ_x, is simply given by

$$\rho_x = \rho_a (R_a/R_x)^3$$

where ρ_a (=1.12 g/cm^3) is the liquid density of PEO,[23] and R_a and R_x are the average radii of the amorphous and crystalline spheres, respectively. The calculated ρ_x's are also listed in Table 2; it can be seen that the calculated densities are unreasonable because they are about 8% and 21% higher than the density of 100% crystalline PEO (=1.24 g/cm^3) for 1K17 and 1K13, respectively. Although spherical form factor yields proper fits to the experimental data, the unreasonably high densities derived from the fits rule out the spherical domain structure in the crystalline blends.

In the crystallization process to achieve the maximum crystallinity, assembly and ordering of PEO blocks into lamellar crystals should tend to transform the spherical microdomains into lamellae- or disklike objects with the crystalline chains aligning along the thickness direction of the disks. Such a microdomain transformation would inevitably perturb the conformations of the corona PB block and homopolymer chains under the constraint of maintaining the normal liquid density in the PB phase. An entropic or elastic force associated with the PB chains thus develops to resist the microdomain deformation induced by crystallization, and the domain structure may be governed by the balance between these two competing forces. If the elastic force dominates over the crystallization driving force to retain the original spherical geometry, the crystallizability of PEO blocks will be depressed compared with that of the corresponding PEO homopolymer, since maintaining the spherical curvature would prohibit the crystalline packing of PEO segments near the domain interface.

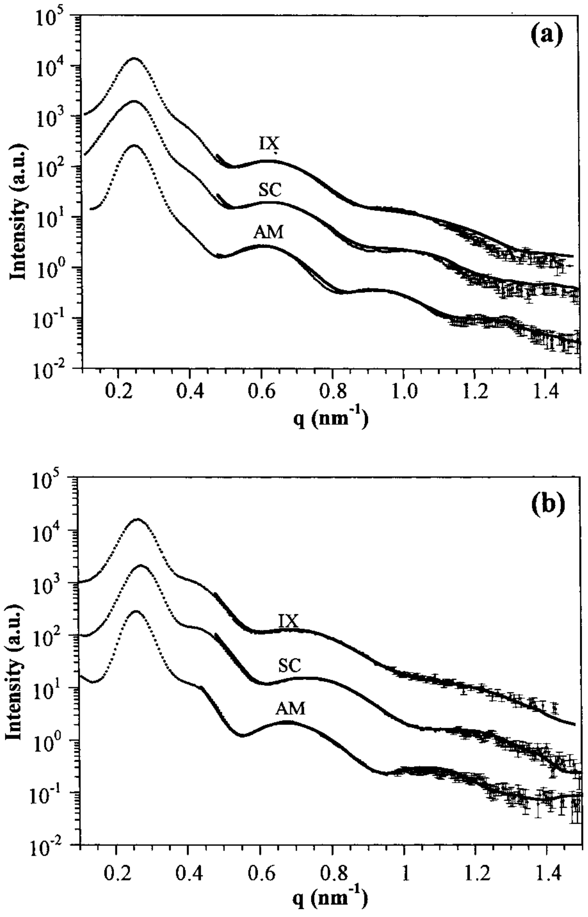

Figure 2. Fits of the experimental form factor profiles by the spherical form factor for amorphous and crystalline (a) 1K17 and (b) 1K13 blends. The solid curves are the calculated profiles.

We have also attempted to fit the observed form factor scattering using the formula for a randomly oriented disk. The fitting is however very poor, indicating the crystalline domains are not disks. The disklike domain structure is further precluded from the real-space morphology observed by TEM (to be shown later).

Since neither driving force can outweigh the other in generating the corresponding favorable domain structure, we now assume that the spheres were deformed into an intermediate structure, i.e., ellipsoid-like objects, arising from the balance between these two driving forces. The form factor for a randomly oriented ellipsoid

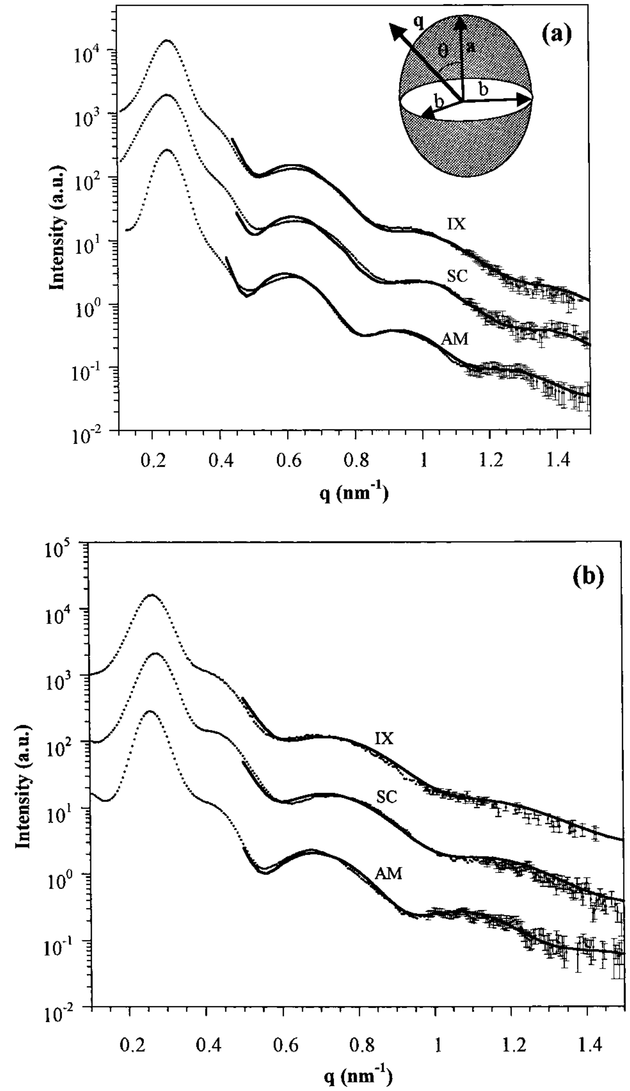

Figure 3. Fits of the experimental form factor profiles by the elliptic form factor for amorphous and crystalline (a) 1K17 and (b) 1K13 blends. The solid curves are the calculated profiles. The model of the ellipsoid assumed is also shown in (a).

with dimensions illustrated in Figure 3a is given by[24]

$$f_e^2(q) = V_e^2 \Delta\rho^2 \exp(-\sigma^2 q^2) \int_0^1 \Phi^2(U^*)\, d\mu \qquad (5)$$

where $\Phi(U^*)$ is given by

$$\Phi(U^*) = \frac{3(\sin U^* - U^* \cos U^*)}{U^{*3}} \qquad (6)$$

where $U^* = q[a^2\mu^2 + b^2(1 - \mu^2)]^{1/2}$ with $\mu = \cos\theta$.

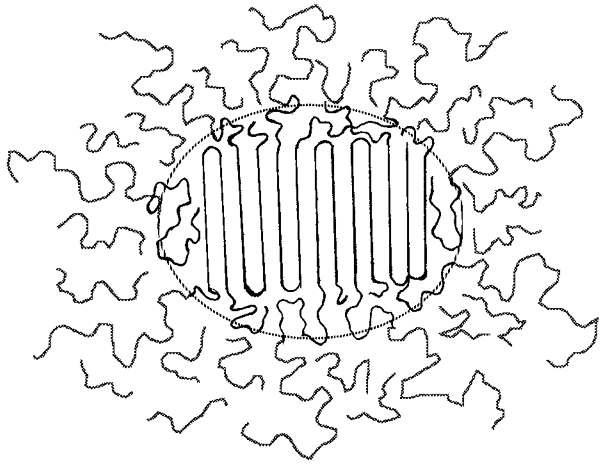

Figure 4. A schematic presentation proposing the structure of the ellipsoid-like crystalline microdomains.

Equation 5 was applied to fit the experimentally observed form factor scattering with considerations of Gaissian distributions of a and b. The results are shown in Figure 3, and the values of $\langle a\rangle$, $\langle b\rangle$, σ_a, and σ_b obtained from the fits are tabulated in Table 3. It can be seen that the elliptic form factor also fits the experimental data well. The densities of the crystalline domains obtained from the fits are also listed in Table 3. In contrast to the results derived from the spherical form factor, reasonable crystalline densities are now predicted. The aspect ratios ($\langle a\rangle/\langle b\rangle$) of the microdomains in the amorphous blends deviate very slightly from unity, showing that the domains are not perfectly spherical because the melt structure has not really attained its equilibrium. The aspect ratio of the crystalline domains increases to approximately 1.3, suggesting that the domains slightly deformed into ellipsoid-like objects upon crystallization. Although both spherical and elliptic form factors fit the data satisfactorily, the density computation rules out the spherical domain structure in the crystalline blends. On the other hand, the good fit plus the density computation based on elliptical form factor adequately verify an ellipsoidal geometry for the crystalline domains. The thickness of the diffuse phase boundary obtained from the fits is displayed in Table 3. The interface in the crystalline samples is thicker, and it may consist of the uncrystalline PEO segments mixed with a minor portion of PB as proposed schematically in Figure 4.

We also attempted to resolve the real-space structure of the ellipsoid-like microdomains through the TEM observation. Figure 5 shows the TEM micrographs of amorphous and crystalline 1K13 blend crystallized by the slow crystallization process. The dark matrix is the PB phase owing to the preferential staining by OsO_4. Since the sample thickness (>30 nm) was larger than

Table 3. Results of the Fit by Elliptic Form Factor for Amorphous and Crystalline PEO-*b*-PB/PB Blends

sample	physical state of PEO blocks[a]	$\langle a\rangle$ (nm)	$\langle b\rangle$ (nm)	σ_a (nm)	σ_b (nm)	σ^2 (nm^2)	t_i (nm)	aspect ratio	ρ_x (g/cm^3)
1K17	amorphous	9.5	9.3	0.8	1.0	0.2	0.79	1.02	
	crystalline (SC)	11.0	8.4	0.7	0.5	0.5	1.25	1.31	1.19
	crystalline (IX)	11.0	8.3	0.7	0.5	0.7	1.48	1.33	1.21
1K13	amorphous	8.2	8.1	0.8	0.9	0.1	0.56	1.01	
	crystalline (SC)	9.6	7.2	1.6	0.6	0.3	0.97	1.33	1.21
	crystalline (IX)	9.7	7.1	1.6	0.7	0.3	0.97	1.37	1.23

[a] SC and IX signify that the crystallizations were conducted by cooling the blends from 85 to −50 °C at −5 °C/min and by isothermal annealing at −50 °C, respectively. [b] t_i is the thickness of the diffuse phase boundary calculated by $t_i = (2\pi)^{1/2}\sigma$.

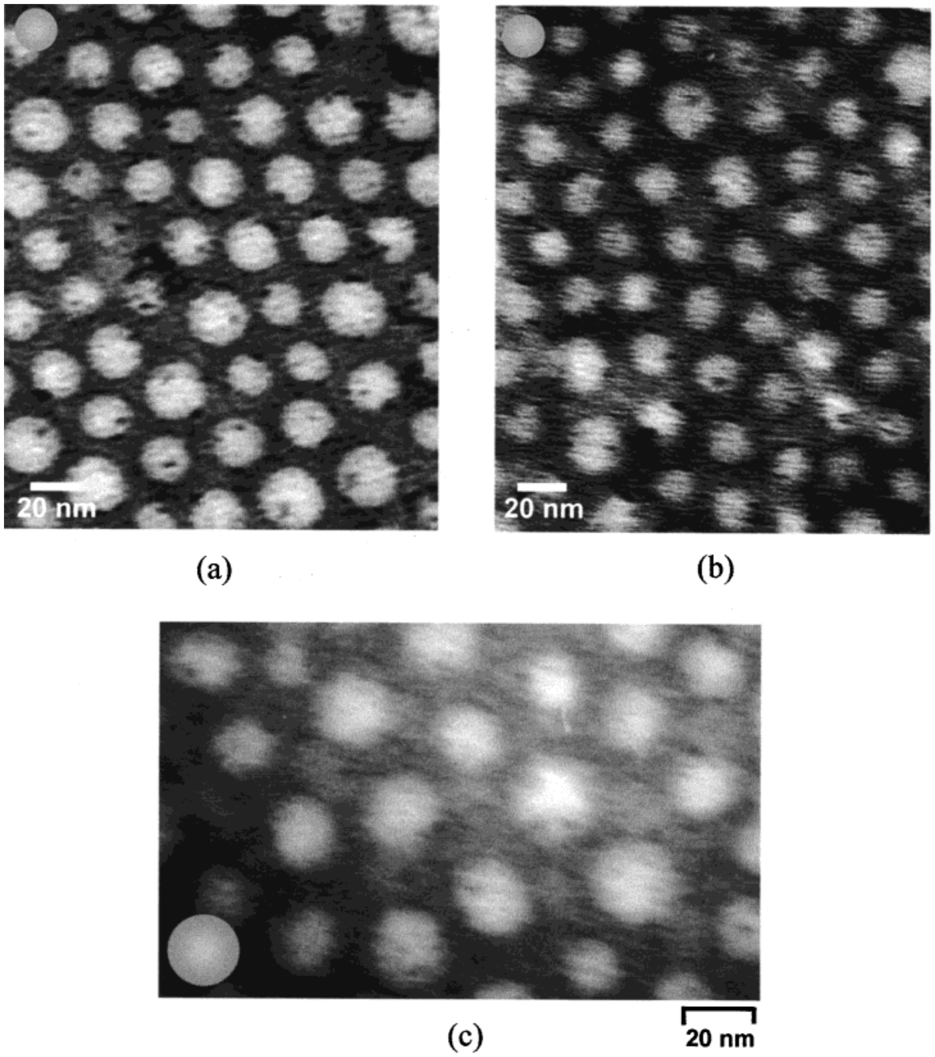

Figure 5. TEM micrographs showing (a) amorphous and (b) crystalline PEO microdomains in 1K13 blend. Spheres were drawn in the corners of the micrographs to help distinguish between the actual shape of the microdomains and that of a sphere. Crystalline microdomains with higher magnification are shown in (c) to better present the images of the ellipsoid-like domains.

the microdomain size, the micrographs basically present the images of the 2-D projections for the whole instead of the sliced domains. Spheres were drawn in the corners of the micrographs to help distinguish between the image of the microdomains and that of a sphere. It is seen that the microdomains in the amorphous sample are virtually spherical with the aspect ratio of ca. 1.05 estimated from the micrograph. The crystalline domains, on the other hand, are smaller due to volume contraction upon crystallization, and a large portion of them are seen to appear like ellipsoids. Since 2-D projections are presented in TEM micrographs, the aspect ratio of the image of an ellipsoid depends on the orientation of the ellipsoid with respect to the direction of the electron beam (e.g., the image of the presently considered ellipsoid would appear like that of a sphere when *a*-axis lies parallel to the electron beam). Therefore, a distribution of aspect ratios should be observed in the TEM micrograph for randomly oriented ellipsoids. The average aspect ratio estimated from the ellipsoid-like images in Figure 5 is 1.27, slightly smaller than that deduced from SAXS.

Concluding Remarks

The present study has shown that the spherical microdomains originally present in the melt state of a PEO-*b*-PB/PB blend system were not preserved upon crystallization, in that the domains slightly deformed into ellipsoid-like objects with the aspect ratio of ca. 1.3. It is noted that the type and extent of morphological perturbation revealed may apply only to the present system with the prescribed molecular weight combination. Since the extent of morphological perturbation should depend on molecular weight, crystallization history, and composition of the system, further study on the effects of these parameters in the intermediate regime shall be indispensable for clarifying the interplay between the driving forces of crystallization and microphase separation.

Acknowledgment. We thank Professor Takeji Hashimoto for offering very helpful comments. This work was supported by the National Science Council of R.O.C. under Grant NSC 90-2216-E-007-035.

References and Notes

(1) Hirata, H.; Ijutsu, T.; Soen, T.; Hashimoto, T.; Kawai, H. *Polymer* **1975**, *16*, 249.
(2) Nojima, S.; Kato, K.; Yamamoto, S.; Ashida, T. *Macromolecules* **1992**, *25*, 2237.
(3) Nojima, S.; Nakano, H.; Ashida, T. *Polymer* **1993**, *34*, 4168.
(4) Rangarajan, P.; Register, R. A.; Fetters, L. J. *Macromolecules* **1993**, *26*, 4640.

(5) Nojima, S.; Nakano, H.; Takahashi, Y.; Ashida, T. *Polymer* **1994**, *35*, 3479.

(6) Nojima, S.; Yamamoto, S.; Ashida, T. *Polym. J.* **1995**, *27*, 673.

(7) Rangarajan, P.; Register, R. A.; Fetters, L. J.; Naylor, S.; Ryan, A. J. *Macromolecules* **1995**, *28*, 1422.

(8) Ryan, A. J.; Hamley, I. W.; Bras, W.; Bates, F. S. *Macromolecules* **1995**, *28*, 3860.

(9) Schnablegger, H.; Rein, D. H.; Rempp, P.; Cohen, R. E. *J. Polym. Eng.* **1996**, *16*, 1.

(10) Nojima, S.; Hashizume, K.; Rohadi, A.; Sasaki, S. *Polymer* **1997**, *38*, 2716.

(11) Ryan, A. J.; Fairclough, J. P. A.; Hamley, I. W.; Mai, S.-M.; Booth, C. *Macromolecules* **1997**, *30*, 1723.

(12) Quiram, D. J.; Register, R. A.; Marchand, G. R.; Ryan, A. J. *Macromolecules* **1997**, *30*, 8338.

(13) Zhu, L.; Chen, Y.; Zhang, A.; Calhoun, B. H.; Chun, M.; Quirk, R. P.; Cheng, S. Z. D.; Hsiao, B. S.; Yeh, F.; Hashimoto, T. *Phys. Rev. B* **1999**, *60*, 10022.

(14) Chen, H.-L.; Wu, J.-C.; Lin, T.-L.; Lin, J. S. *Macromolecules* **2001**, *34*, 6936.

(15) Chen, H.-L.; Hsiao, S.-C.; Lin, T.-L.; Yamauchi, K.; Hasegawa, H.; Hashimoto, T. *Macromolecules* **2001**, *34*, 671.

(16) Winey, K. I.; Thomas, E. L.; Fetters, L. *Macromolecules* **1992**, *25*, 2645.

(17) Tanaka, H.; Hasegawa, H.; Hashimoto, T. *Macromolecules* **1991**, *24*, 240.

(18) Medellin-Rodriguez, F. J.; Philips, P. J.; Lin, J. S. *Macromolecules* **1996**, *29*, 7491.

(19) Loo, Y.-L.; Register, R. A.; Ryan, A. J. *Phys. Rev. Lett.* **2000**, *84*, 4120.

(20) Chen, H.-L.; Huang, Y.-Y.; Hashimoto, T., manuscript in preparation.

(21) Roe, R.-J. *Methods of X-ray and Neutron Scattering in Polymer Science*; Oxford University Press: New York, 2000.

(22) Hashimoto, T.; Tanaka, H.; Hasegawa, H. *Macromolecules* **1990**, *23*, 4378.

(23) *Polymer Handbook*, 3rd ed.; Brandrup, J., Immergut, E. H., Eds.; Wiley: New York, 1989.

(24) Feigin, L. A.; Svergun, D. I. *Structure Analysis by Small-Angle X-ray and Neutron Scattering*; Plenum Press: New York, 1987.

MA011748K